INTERNATIONAL JOURNAL FOR NUMERICAL METHODS IN FLUIDS
Int. J. Numer. Meth. Fluids 2003; **43**:1199–1220 (DOI: 10.1002/fld.542)

Fluid dynamic numerical simulation of a gas phase polymerization reactor

Anne Gobin[1,*,†], Hervé Neau[1], Olivier Simonin[1,2], Jean-Richard Llinas[3], Vince Reiling[3] and Jean-Loïc Sélo[3]

[1]*Institut de Mécanique des Fluides de Toulouse (IMFT)—UMR CNRS-INPT-UPS 5502 Allée du Pr. Camille Soula, 31400 Toulouse, France*
[2]*Département Mécanique des Fluides et Transferts Thermiques, EDF R&D 6 Quai Watier, 78000 Chatou, France*
[3]*Centre de Recherche et Technologie—BP Chemicals SNC BP no 6, 13117 Lavéra, France*

SUMMARY

This article presents preliminary fluid dynamic simulation results of ethylene polymerization dense fluidized bed using the two-phase flow numerical code ESTET-ASTRID developed by Electricité de France for CFB boilers and based on the two-fluid modelling approach. The continuous phase consists of gas and the dispersed phase consists of catalyst particles. The particle fluctuating motion is modelled using two-separate transport equations, on the particle kinetic energy and the fluid–particle covariance, developed in the frame of kinetic theory of granular medium accounting for particle–particle and fluid–particle interactions. Time-dependent 2D and 3D simulations have been performed for industrial and pilot reactor operating conditions. The numerical predictions are in good qualitative agreement with the observed behaviour in terms of bed height, pressure drop and mean flow organization, such as the down falling of the PE particle layer along the walls. Moreover, these simulations help to provide information about instantaneous and time-averaged solid concentration and velocity fields. Characteristic mechanisms and influence of model closure assumptions on flow predictions are also investigated. Finally, such numerical simulations look very powerful, when validated on exhaustive data collection, to improve design and performance of industrial facilities and to provide insight into the complex physical mechanisms involved. Copyright © 2003 John Wiley & Sons, Ltd.

KEY WORDS: dense fluidized bed; industrial polymerization reactor; gas–particle flow; two-phase flow modelling

1. INTRODUCTION

The project, involving BP (Polyethylene Business), Electricité de France (EDF R&D) and the 'Institut de Mécanique des Fluides de Toulouse' (IMFT), consists inthe fluid dynamic

* Correspondence to: A. Gobin, Institut de Mécanique des Fluides de Toulouse (IMFT) - UMR CNRS-INPT-UPS 5502, Allée du Pr. Camille Soula, 31400 Toulouse, France.
† E-mail: gobin@imft.fr

Contract/grant sponsor: Calcul en Midi-Pyrénées; contract/grant number: P0111

Received 3 March 2002
Revised 19 February 2003

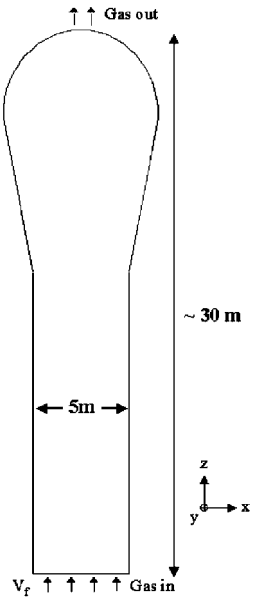

Figure 1. Industrial reactor sketch.

numerical modelling of industrial polyethylene (PE) reactors. The PE is obtained by catalytic polymerization of ethylene, occurring in a fluidized bed reactor. The bubbling of the gas into the particle bed leads to an efficient contact between the ethylene and the catalyst. It prevents also hot spot appearance by a constant heat homogenization. The geometry used in this work, representing an operational BP reactor, is cylindrical with a bulb at the top, about 30 m high and 5 m wide as shown in Figure 1.

The operating conditions used in the frame of this project do not correspond to a standard production situation. Nevertheless some experiments were done in these conditions to enable the comparison with the numerical predictions. Given the reactor dimensions, this study aims at modelling the physical behaviour of such fluidized bed in a relative short computing time.

2. PRESENTATION OF THE SIMULATIONS

All the simulations are completed by ASTRID, a two-phase flow numerical code developed by Electricité de France and based on the two-fluid modelling approach [1]. The numerical simulations results will then be compared to measurements made in the site of BP in Lavéra.

2.1. Two-fluid model

The two-fluid model consists in an Eulerian approach for both phases. Mean separate equations are solved for each phase and coupled through interface transfer terms (mass, momentum and enthalpy). The turbulent motion of the continuous phase is predicted by a two-equation single-phase model—the so-called q^2-ε eddy viscosity model—with additional terms expressing the

interactions with the dispersed phase. The modelling of the dispersed phase fluctuating motion is achieved by two separate transport equations: on the particle kinetic energy and on the fluid–particle covariance, developed in the frame of kinetic theory of dry granular medium [2–4] with an original approach to account simultaneously for particle–particle and fluid–particle interaction mechanisms [5–7]. The model implies non-reactive flow and a unique equivalent diameter for the dispersed phase. It includes also a hard sphere inelastic collision model with, as only parameter, the inelastic restitution coefficient e_c. Such a modelling approach has been applied previously for the prediction of dense fluidized beds at laboratory scale and validated by comparison with detailed experimental data [8–10]. In the present work, the main interest is to discuss the application of the modelling approach at an industrial scale for representative flow conditions and, therefore, no emphasis is put on the motivation and theoretical derivation of the model closures and the analysis of the predictions will remain very qualitative due to the lack of available experimental data. Using statistical averaging procedures, the balance equations for isothermal gas–solid flows can be written as follows.

2.1.1. Mass balance.

$$\frac{\partial}{\partial t}\alpha_k\rho_k + \frac{\partial}{\partial x_i}\alpha_k\rho_k U_{k,i} = 0 \tag{1}$$

$\alpha_k = \langle\chi_k\rangle$ is the fraction rate for the gas ($k=1$) and the solid ($k=2$) verifying $\sum_{k=1}^{2}\alpha_k = 1$, $\langle\,.\,\rangle$ is an ensemble averaging operator and χ_k the local instantaneous phase distribution function, $U_{k,i} = \langle u_i\rangle_k$ represents the mean velocity of phase k with $\langle g\rangle_k$ being the conditional phase average of any variable g, $\alpha_k\rho_k\langle g\rangle_k = \langle\chi_k\rho g\rangle$.

2.1.2. Momentum balance.

$$\alpha_k\rho_k\frac{\partial U_{k,i}}{\partial t} + \alpha_k\rho_k U_{k,j}\frac{\partial U_{k,i}}{\partial x_j} = -\alpha_k\frac{\partial P_1}{\partial x_i} + \alpha_k\rho_k g_i + I_{k,i} + \frac{\partial}{\partial x_j}[-\alpha_k\rho_k\langle u''_{k,i}u''_{k,j}\rangle_k + \Theta_{k,ij}] \tag{2}$$

with $u''_{k,i} = u_i - u_{k,i}$ and $\langle\rho u''_{k,i}\rangle_k = 0$.
$\langle u''_{k,i}u''_{k,j}\rangle_k$ represents the fluid turbulent Reynolds stress tensor ($k=1$) or particle kinetic stress tensor ($k=2$), $\Theta_{k,ij}$ the fluid viscous stress tensor ($k=1$) or the particle collisional stress tensor ($k=2$) and $I_{k,i}$ the mean interphase momentum transfer for phase k, after subtraction of the contribution of the mean fluid pressure gradient, and verifies $\sum_{k=1}^{2} I_{k,i} = 0$.

The interphase momentum transfer is given by

$$I_{1,i} = -I_{2,i} = \alpha_2\rho_2\frac{1}{\tau_{12}^{F}}V_{r,i} \tag{3}$$

τ_{12}^{F} is the mean particle relaxation time accounting for the drag force on the particles and is expressed using two different experimental laws depending on the value of α_2.: Wen and Yu [11] in dilute flows and Ergun's law in dense flows. But, in contrast with previous studies [4, 7], this work showed that to avoid inconsistent results for large particle Reynolds number

values ($Re_p \geqslant 100$), the transition from one law to another cannot be done at a constant value of $\alpha_2 = 20\%$ and, insuring continuity between the two expressions, τ_{12}^{F} is written:

$$\frac{1}{\tau_{12}^{\mathrm{F}}} = \frac{3\rho_1}{4\rho_2} \frac{\langle |\mathbf{v}_r| \rangle_2}{\bar{d}} \mathrm{Min}[C_{D,WY}; C_{D,\mathrm{Erg}}]$$

$$\text{with} \quad C_{D,\mathrm{Erg}} = 200 \frac{\alpha_2}{Re_p} + \frac{7}{3} \quad Re_p = \frac{\alpha_1 \langle |\mathbf{v}_r| \rangle_2 \bar{d}}{\nu_1}$$

$$\text{and} \quad C_{D,WY} = \frac{24}{Re_p}[1 + 0.15 Re_p^{0.687}] \alpha_1^{-1.7} \quad Re_p < 1000$$

$$C_{D,WY} = 0.44 \alpha_1^{-1.7} \quad Re_p \geqslant 1000$$

$V_{r,i}$ is the mean relative velocity, written in terms of the separate mean phase velocities, $U_{k,i}$, and the fluid–particle turbulence drift velocity, $V_{d,i}$, due to the turbulent correlation between the instantaneous particle distribution and the fluid velocity field,

$$V_{r,i} = (U_{2,i} - U_{1,i}) - V_{d,i}$$

$V_{d,i}$ is accounting for the turbulence transport of the dispersed phase by the fluid turbulence [12] and is modelled using the following gradient approximation:

$$V_{d,i} = -D_{12}^t \left[\frac{1}{\alpha_2} \frac{\partial \alpha_2}{\partial x_i} - \frac{1}{\alpha_1} \frac{\partial \alpha_1}{\partial x_i} \right]$$

with the dispersion coefficient proportional to the fluid–particle velocity covariance $q_{12} = \langle u''_{1,i} u''_{2,i} \rangle_2$ and an eddy–particle interaction time, τ_{12}^t, characterizing the fluid turbulence experienced ('viewed') by the particles.

This fluid–particle turbulent drift velocity allows to ensure the consistency of the model for the limit case of very small particles which behave as tracers in the gas and becomes fully negligible for coarse particles when the particle relaxation time τ_{12}^{F} is much larger than the fluid turbulence time macroscales.

2.1.3. Modelling of the continuous phase turbulence: q^2-ε model. The computation of the turbulence characteristics is achieved by considering only the instantaneous fluid motions at large scales with respect to the particle diameter. The fluid turbulent Reynolds stress tensor is written in the frame of the turbulent eddy viscosity assumption:

$$\langle u''_{1,j} u''_{1,i} \rangle_1 = -\nu_1^t \left[\frac{\partial U_{1,i}}{\partial x_j} + \frac{\partial U_{1,j}}{\partial x_i} \right] + \frac{2}{3} \delta_{ij} \left[\frac{1}{2} q_1^2 + \nu_1^t \frac{\partial U_{1,m}}{\partial x_m} \right] \tag{4}$$

where the practical expression for the turbulent viscosity ν_1^t is derived from the separate transport equations governing the fluid Reynolds stress tensor components, assuming that the tensor anisotropy remains small and locally in equilibrium. This approach allows to generalize the single-phase closure assumption such as

$$\nu_1^t = \frac{2}{3} q_1^2 \tau_1^t \left[1 + C_{12} \frac{\alpha_2 \rho_2}{\alpha_1 \rho_1} \frac{\tau_{12}^t}{\tau_{12}^{\mathrm{F}}} \left(1 - \frac{q_{12}}{2 q_1^2} \right) \right]^{-1}$$

In addition, the transport equations for the fluid turbulent kinetic energy q_1^2 and dissipation rate ε make appear two specific terms accounting for the effect of the particles ('two-way coupling'),

$$\Pi_{q_1} = -\frac{\alpha_2 \rho_2}{\tau_{12}^{\mathrm{F}}}[2q_1^2 - q_{12} - V_{d,i} V_{r,i}] \quad \Pi_{\varepsilon_1} = C_{\varepsilon,3} \frac{\varepsilon_1}{q_1^2} \Pi_{q_1}$$

We can notice that the above proposed modifications of the single-phase turbulent closure assumptions due to the particle presence lead to a damping effect of the fluid turbulence in gas–particle flow, generally, which increases with the solid loading ratio. As a consequence the fluid turbulence in the bottom part of the polymerization reactor is found to have a very poor influence on the flow predictions.

2.1.4. Modelling of the fluid–particle velocity correlations: q_{12} model. The modelling of the fluid–particle velocity correlation tensor is using an eddy-viscosity assumption, or Boussinesq approximation, supplemented by a transport equation for the fluid–particle velocity covariance q_{12} [12]. Such closure assumptions and q_{12} transport equation are derived from the separate transport equations governing the fluid–particle correlation tensor components, assuming that the tensor anisotropy remains small and locally in equilibrium, and are written:

$$\langle u''_{1,i} u''_{2,j} \rangle_2 = \frac{1}{3} q_{12} \delta_{ij} + \frac{\eta_r}{1+\eta_r} \left[\langle u''_{1,i} u''_{1,j} \rangle_1 - \frac{2}{3} q_1^2 \delta_{ij} \right] - \frac{\nu_{12}^t}{1+\eta_r} \left[\frac{\partial U_{1,i}}{\partial x_j} + \frac{\partial U_{2,j}}{\partial x_i} - \frac{1}{3} \frac{\partial U_{1,m}}{\partial x_m} \delta_{ij} - \frac{1}{3} \frac{\partial U_{2,m}}{\partial x_m} \delta_{ij} \right] \tag{5}$$

ν_{12}^t is the fluid–particle turbulent viscosity accounting for the particle momentum transport by the fluid turbulence.

$$\alpha_2 \rho_2 \frac{\partial q_{12}}{\partial t} + \alpha_2 \rho_2 U_{2,i} \frac{\partial q_{12}}{\partial x_i} = \frac{\partial}{\partial x_i} \left(\alpha_2 \rho_2 \frac{\nu_{12}^t}{\sigma_q} \frac{\partial q_{12}}{\partial x_i} \right) - \alpha_2 \rho_2 \varepsilon_{12} + \Pi_{q_{12}} - \alpha_2 \rho_2 \left[\langle u''_{1,i} u''_{2,j} \rangle_2 \frac{\partial U_{2,i}}{\partial x_j} + \langle u''_{1,j} u''_{2,i} \rangle_2 \frac{\partial U_{1,i}}{\partial x_j} \right] \tag{6}$$

with the fluid–particle covariance dissipation rate due to viscous dissipation and crossing-trajectory effects,

$$\varepsilon_{12} = \frac{q_{12}}{\tau_{12}^t}$$

and the inter-phase interaction term

$$\Pi_{q_{12}} = -\alpha_2 \rho_2 \frac{1}{\tau_{12}^{\mathrm{F}}} \left[(q_{12} - 2q_1^2) + \frac{\alpha_2 \rho_2}{\alpha_1 \rho_1} (q_{12} - 2q_2^2) \right]$$

2.1.5. Modelling of the particle fluctuating motion: q_2^2 model. The particle fluctuating motion induces two very different contributions in the effective stress of the dispersed phase [13]. The particle kinetic stress tensor $\langle u''_{2,i}u''_{2,j}\rangle_2$ represents the mean transport of particle momentum by the velocity fluctuations, and is found to be dominant in dilute flows. In contrast the particle collisional stress tensor $\Theta_{2,ij}$ represents the mean transport of particle momentum through the inter-particle collisions and is the dominant effect in dense flows: $\alpha_2 > 10\%$, typically.

The modelling of the kinetic and collisional parts of the effective particle stress tensor are derived in the frame of the classical theory of dry granular media [3] but supplemented by the effect of the intersticial fluid by accounting for the drag force and the fluid turbulence influence in the derivation of the particle kinetic energy equation and transport properties: viscosity and diffusivity [12].

The Boussinesq approximation for the particle kinetic stress tensor is derived from the separate transport equations governing the corresponding components, assuming that the tensor anisotropy remains small and locally in equilibrium,

$$\langle u''_{2,j}u''_{2,i}\rangle_2 = -\nu_2^{\mathrm{kin}}\left[\frac{\partial U_{2,i}}{\partial x_j} + \frac{\partial U_{2,j}}{\partial x_i}\right] + \frac{2}{3}\,\delta_{ij}\left[q_2^2 + \nu_2^{\mathrm{kin}}\frac{\partial U_{2,m}}{\partial x_m}\right] \tag{7}$$

Such an approach leads to the following form of the particle kinetic viscosity ν_2^{kin} which accounts directly for the combined effects of different mechanisms such as: the transport of particle momentum by the fluid turbulence and by their own random motion, the competition between drag and collision influences on the mean free path of the particles,

$$\nu_2^{\mathrm{kin}} = \left[\nu_{12}^t + \frac{\tau_{12}^{\mathrm{F}}}{2}\,\frac{2}{3}\,q_2^2(1+\alpha_2 g_0 \Phi_c)\right]\left(1 + \frac{\tau_{12}^{\mathrm{F}}}{2}\,\frac{\sigma_{\mathrm{c}}}{\tau_2^{\mathrm{c}}}\right)^{-1}$$

The particle kinetic energy equation is obtained by summation of the separate transport equations governing the normal kinetic stress tensor components and is written,

$$\alpha_2\rho_2\frac{\partial q_2^2}{\partial t} + \alpha_2\rho_2 U_{2,i}\frac{\partial q_2^2}{\partial x_i} = \frac{\partial}{\partial x_j}\left(\alpha_2\rho_2[K_2^{\mathrm{kin}} + K_2^{\mathrm{col}}]\frac{\partial q_2^2}{\partial x_j}\right) - (\alpha_2\rho_2\langle u''_{2,i}u''_{2,j}\rangle_2 + \Theta_{2,ij})\frac{\partial U_{2,i}}{\partial x_j} - \alpha_2\rho_2\varepsilon_2 + \Pi_{q_2} \tag{8}$$

with the particle kinetic energy dissipation rate due to inelastic collisions

$$\varepsilon_2 = \frac{1}{3}(1-e_{\mathrm{c}}^2)\frac{q_2^2}{\tau_2^{\mathrm{c}}}$$

and the inter-phase turbulent kinetic energy transfer rate

$$\Pi_{q_2} = -\alpha_2\rho_2\,\frac{1}{\tau_{12}^{\mathrm{F}}}(2q_2^2 - q_{12})$$

Following Boelle *et al.* [14], the theoretical model derivation of the collisional part of the effective particle stress tensor is not affected by the interstitial fluid and so the corresponding

Table I. Closure assumptions of the two-fluid model.

$\langle \lvert \mathbf{v}_r \rvert \rangle_2 = \sqrt{V_{r,i} V_{r,i} + \langle v^t_{r,i} v^t_{r,i} \rangle_2}$	
$D^t_{12} = \tau^t_{12} \dfrac{1}{3} q_{12}$	$\eta_r = \tau^t_{12} / \tau^{\mathrm{F}}_{12}$
$\tau^t_1 = \dfrac{3}{2} C_\mu \dfrac{q_1^2}{\varepsilon_1}$	$\tau^t_{12} = \dfrac{\tau^t_1}{\sigma_1} \left[1 + C_\beta \dfrac{\lfloor V_r \rfloor^2}{\frac{2}{3} q_1^2} \right]^{-\frac{1}{2}}$
$\tau^c_2 = \left(6 \dfrac{\alpha_2 g_0}{\bar{d}} \sqrt{\dfrac{16}{\pi} \dfrac{2}{3} q_2^2} \right)^{-1}$	$\nu^t_{12} = \dfrac{1}{3} \tau^t_{12} q_{12}$
$\lambda_2 = \dfrac{4}{3} \alpha_2^2 \rho_2 \bar{d} g_0 (1 + e_c) \sqrt{\dfrac{2}{3} \dfrac{q_2^2}{\pi}}$	
$K^{\mathrm{col}}_2 = \alpha_2 g_0 (1 + e_c) \left(\dfrac{6}{5} K^{\mathrm{kin}}_2 + \dfrac{4}{3} \bar{d} \sqrt{\dfrac{2}{3} \dfrac{q_2^2}{\pi}} \right)$	
$K^{\mathrm{kin}}_2 = \left[\dfrac{1}{3} \tau^t_{12} q_{12} + \dfrac{5}{9} \tau^{\mathrm{F}}_{12} \dfrac{2}{3} q_2^2 (1 + \alpha_2 g_0 \varphi_c) \right] \left(1 + \dfrac{5}{9} \tau^{\mathrm{F}}_{12} \dfrac{\xi_c}{\tau^c_2} \right)^{-1}$	
$g_0 = \left(1 - \dfrac{\alpha_2}{\alpha_m} \right)^{-2.5 \alpha_m}$	
$\Phi_c = \dfrac{2}{5} (1 + e_c)(3e_c - 1)$	$\varphi_c = \dfrac{3}{5} (1 + e_c)^2 (2e_c - 1)$
$\xi_c = \dfrac{(1 + e_c)(49 - 33 e_c)}{100}$	$\sigma_c = \dfrac{(1 + e_c)(3 - e_c)}{5}$

Boussinesq approximation is nearly identical to the one developed for dry granular media [3].

$$\Theta_{2,ij} = \left[\frac{2}{3} \alpha_2 \rho_2 q_2^2 (2 \alpha_2 g_0 (1 + e_c)) - \lambda_2 \frac{\partial U_{2,m}}{\partial x_m} \right] \delta_{ij} - \alpha_2 \rho_2 \nu^{\mathrm{col}}_2 \left[\frac{\partial U_{2,i}}{\partial x_j} + \frac{\partial U_{2,j}}{\partial x_i} - \frac{2}{3} \frac{\partial U_{2,m}}{\partial x_m} \delta_{ij} \right] \tag{9}$$

with the collisional viscosity

$$\nu^{\mathrm{col}}_2 = \frac{4}{5} \alpha_2 g_0 (1 + e_c) \left(\nu^{\mathrm{kin}}_2 + \bar{d} \sqrt{\frac{2}{3} \frac{q_2^2}{\pi}} \right)$$

Missing closure assumptions are given explicitly in Table I and the values of the parameters of the fluid turbulence model are given in Table II.

2.2. Numerical resolution method

The code ASTRID [6] deals with structured meshes in cartesian or curvilinear coordinates. Pressure and volumetric fraction are located at the centre of each cell of the collocated

Table II. Parameters of the fluid turbulence model.

C_μ	$C_{\varepsilon,3}$	C_{12}	σ_q	σ_ε	σ_1	C_β
0.09	1.2	0.34	1.0	1.3	1.0	1.8

'velocity grid' and formed a half-staggered 'pressure grid'. Mass conservation equations are solved with a finite volume method whereas the other equations are solved with a finite difference method.

Separate mass conservation of both phase is insured by solving the transport equation of the dispersed phase mass concentration: $X_2 = \alpha_2 \rho_2$ and a Poisson type equation of the mean gas pressure. This late equation is derived in the frame of the SIMPLE algorithm methodology, from the volume conservation equation of the two-phase mixture and the phase momentum transport equations, allowing an implicit coupling of the mean interphase transfer terms.

2.3. Experimental data

The experimental measurements are traditionally difficult to carry out in an industrial reactor. In a first stage, validation was performed using pressure drop profile in the bed. In the framework of Ergun's law, the mean solid volumetric fraction could be deduced from this pressure drop. Indeed, in dense fluidized beds, the pressure drop is mainly due to the weight of the particles of the bed. The effect of the collisions, and others rubbing on the walls of the reactor, on the pressure drop is negligible. This leads to the following expression:

$$\frac{\Delta P}{L} = \alpha_2(\rho_2 - \rho_1)g \tag{10}$$

where L corresponds to the height difference between the two captors of pressure.

3. DESCRIPTION AND RESULTS OF THE REFERENCE CASE

3.1. Physical and numerical data

The continuous phase is hydrocarbon gas, at 80°C and 20 bar, with a density and a kinetic viscosity of respectively $\rho_g = 20\,\mathrm{kg/m^3}$ and $v_g = 7^{*}10^{-7}\,\mathrm{m^2/s}$. The dispersed phase consists of spherical particles whose mean diameter is supposed to be uniform and constant and equal to 1.3 mm. The density of the solid is $\rho_p = 850\,\mathrm{kg/m^3}$. The superficial fluidization velocity U_f is about 0.5 m/s and represents the inlet gas velocity in the empty reactor. The particle Reynolds number value computed from the above physical data assuming a homogeneous expanded bed, $Re_p = U_f \bar{d}/v_1$, is about 1000.

The reference case is a 2D simulation. The mesh (49*226 cells, i.e. $\Delta x_{\mathrm{mean}} = 10$ cm and $\Delta z_{\mathrm{mean}} = 13$ cm) must be neither too large, to capture the structures of the flow, nor too small to allow a feasible simulation time.

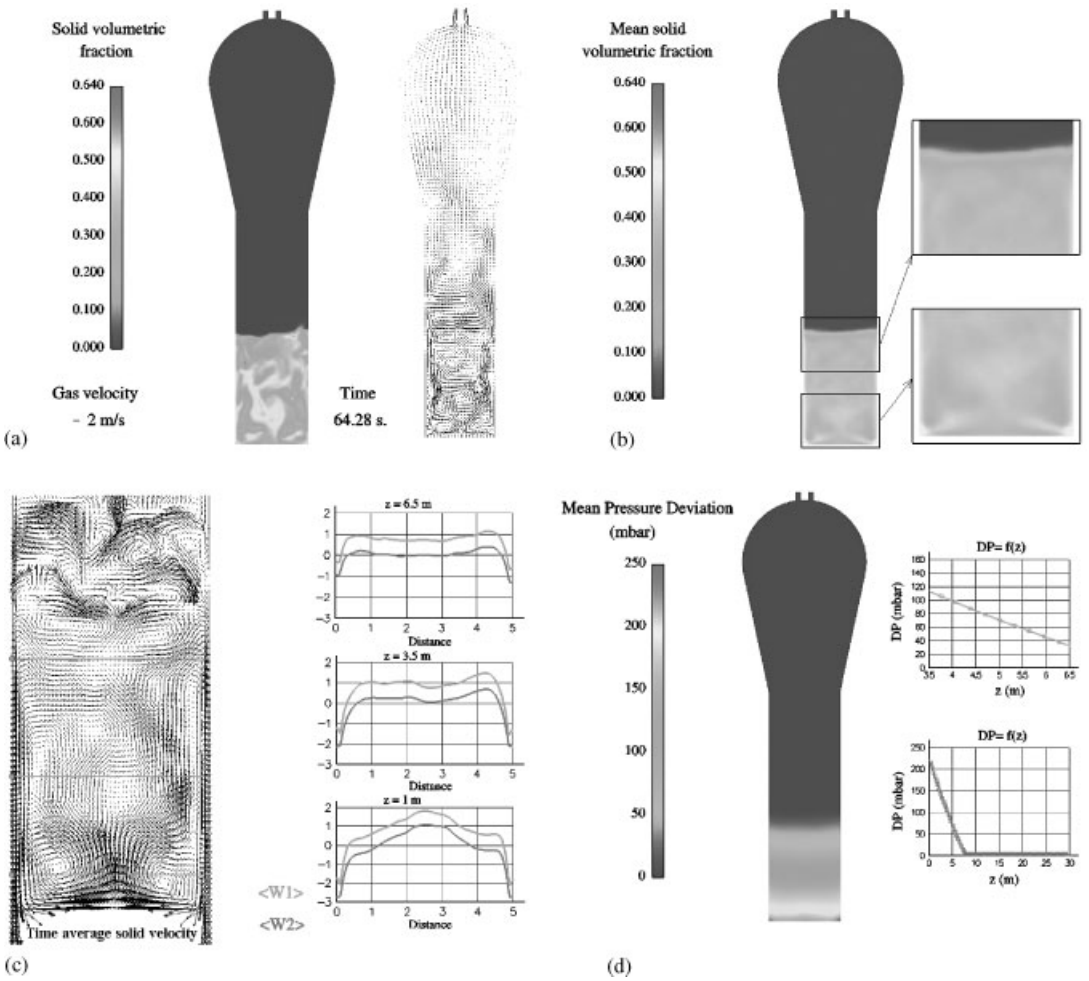

Figure 2. Simulation results of the reference case.

3.2. *Simulation results*

The reactor was simulated for about 80 s with an average time step of 10^{-2} s. The maximal Courant number value $N_C = U_x * \Delta t / \Delta x$ is typically equal to 0.3, which is optimum for a good behaviour of the calculations. Instantaneous and time averaged results are shown in Figure 2. The total catalyst mass is about 2500 kg/m^2, which corresponds to a 8 m high bed with a mean solid volumetric fraction of about 35%. As expected for dense fluidized bed predictions [8–10], the computed flow is fully unsteady with the appearance of bubbles rising to explode at the surface of the bed. The time averaged solid velocity field represented in Figure 2(c) shows recirculation loops with a central upward jet and downward solid flows near the wall of the reactor. These recirculations are also underlined by the gas and solid vertical time averaged velocities which are negative near the walls and positive in the centre. The gas

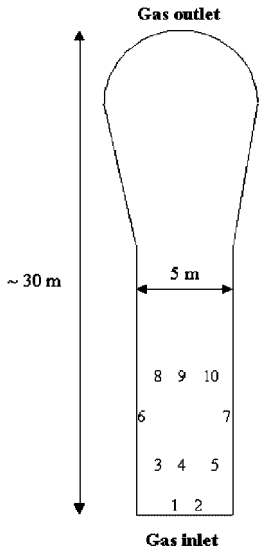

Figure 3. Position of the numerical probes in the reactor.

vertical velocity ranges from -2 m/s to 4 m/s. A smaller maximal upward particle velocity of about 2.5 m/s and a larger maximal downward particle velocity of about -2.5 m/s are due to the drift between the two phases induced by gravity.

3.3. Discussion

The comparison between numerical and experimental results must be done from statistically steady state simulations. The simulations can be assimilated to a 'numerical experiment' with a transient state and a steady one. So it is crucial to characterize the time from when this steady state was reached. A simulation has been done for 120 s and 'numerical probes' were positioned in the reactor to follow the time evolution of some parameters, such as particle and gas velocities, solid volumetric fraction and pressure. Figure 3 demonstrate the position of the probes in the bed and the Figure 4 shows the evolution of the solid volumetric fraction and the pressure at probe 7.

From these instantaneous signals, several successive time averages over 20 s realizations were worked out, each realization representing samples of 4000 points with a constant time step equal to 0.005 s. The steady state, defined by a quasi non-evolution of the mean values, can be assumed to be reached after about 50 s. A further study is carried out to validate this average calculations by computing the characteristic time macro-scales of the large scales flow mechanisms from the Eulerian time correlation functions.

The available experimental value was the pressure drop inside the catalytic bed measured in the bottom part of the reactor close to wall. So Figures 5 and 6 present the pressure drop time evolution and its time averaged value predicted at about 50 cm from the wall.

Both figures give a time averaged pressure drop of 85 mbar, the experimental value ranging from 90 to 110 mbar. This discrepancy between the numerical and the experimental pressure drops is very reasonable given the approximations done and especially the description of the

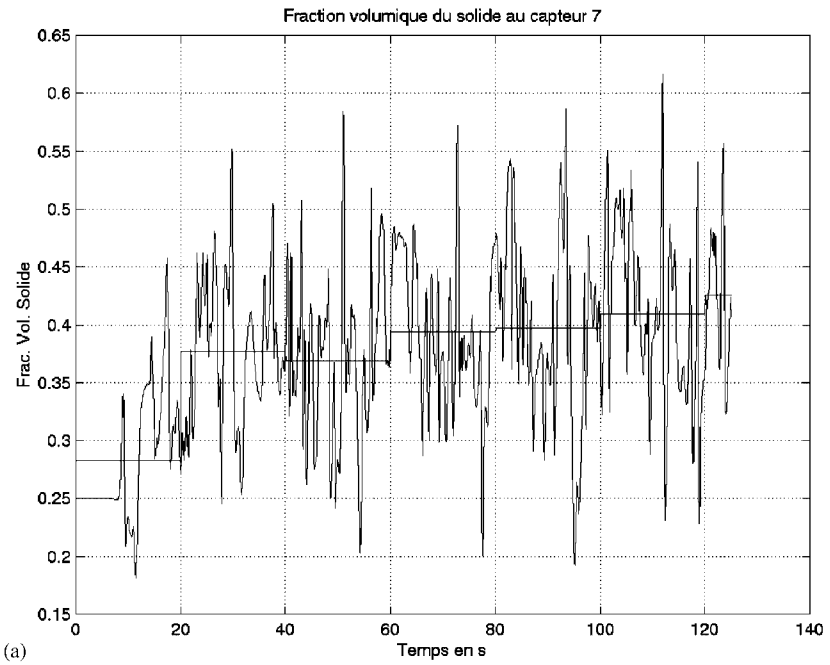

(a)

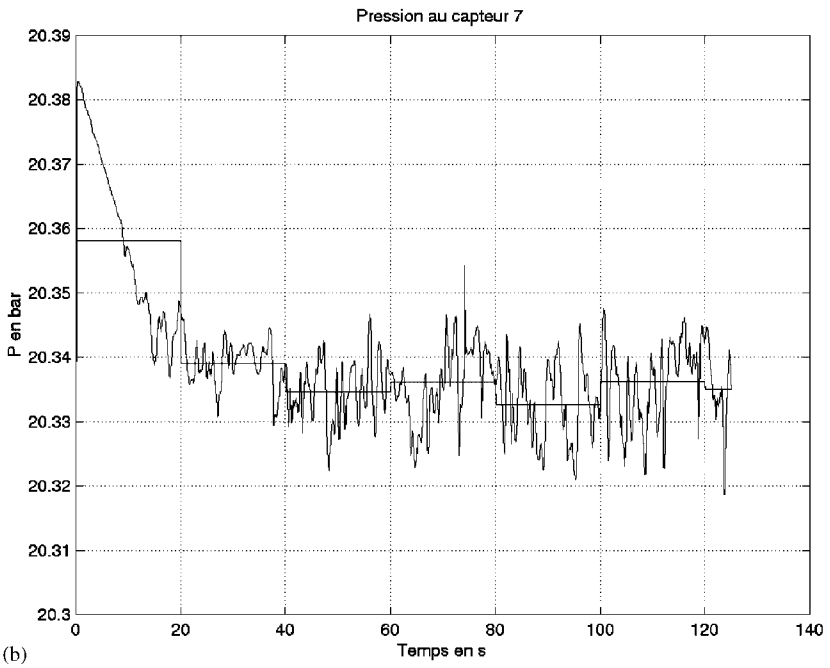

(b)

Figure 4. Time evolution of two parameters at probe 7.

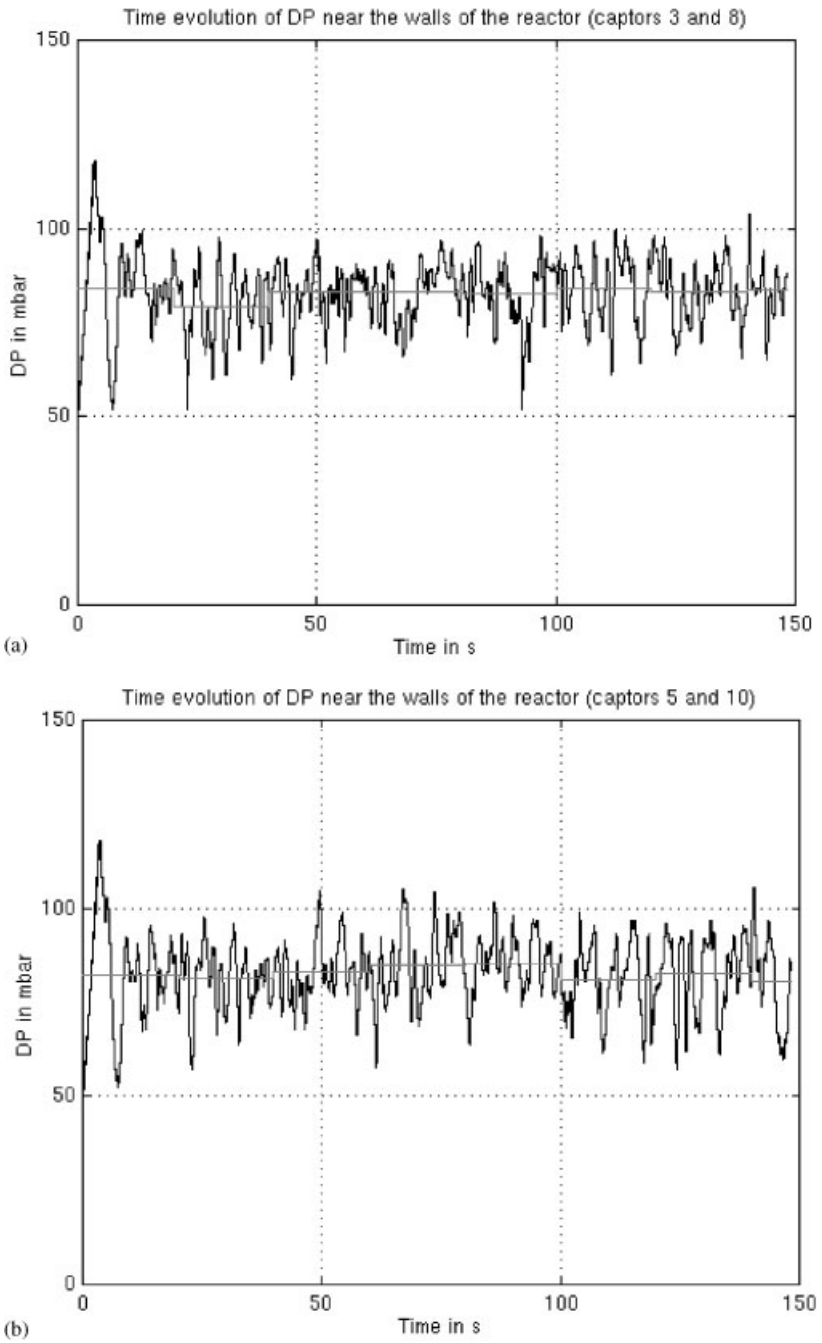

Figure 5. Numerical pressure drop measurement.

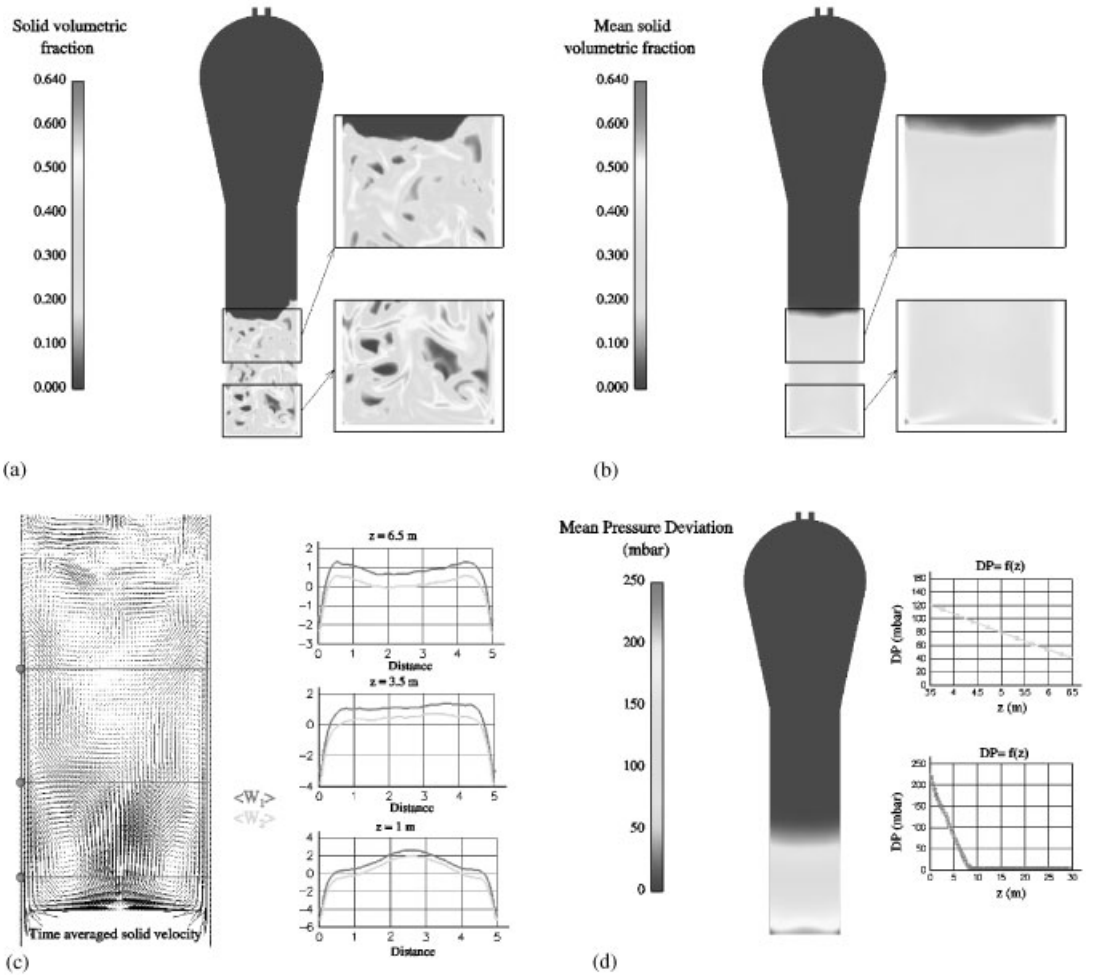

Figure 6. Results of the refined mesh case.

particles. Indeed, the two-phase flow numerical code ESTET-ASTRID has been used in this study without any model parameter adjustment. The equivalent mean diameter was determined experimentally in the framework of Ergun's law. But viewing the solid phase as an ensemble of spherical particles with a unique equivalent diameter is a very rough assumption and a more precise description of the particles may imply some changes in the bed height and therefore in the pressure drop. In addition to this pressure drop, the mean behaviour of the flow, showing recirculation loops inside the reactor, agrees also very well with the present process knowledge, even if the velocities in the near-wall region seem to be overestimated. Nevertheless this study leads us to validate at least qualitatively the 2D simulation of this industrial reactor. Finally, a more extensive experimental campaign is on going and will allow much more detailed validations.

Table III. Simulation results for the reference and the refined cases.

	Reference case	Case with refined mesh
Bed height (m)	8.0	7.7
Mean solid volumetric fraction	0.34	0.36
Pressure drop (3.5–6.5 m) (mbar)	85	89
Maximal time averaged gas velocity (upwards) (m/s)	3.9	3.9
Maximal time averaged gas velocity (downwards) (m/s)	−2.0	−4.8
Maximal time averaged particle velocity (upwards) (m/s)	2.4	2.7
Maximal time averaged particle velocity (downwards) (m/s)	−2.6	−5.1

4. SENSITIVITY TO THE MESH

The studied fluidized bed is very large (30 m high). To get a feasible computing time, a rather large grid was preferred ($\Delta x_{\text{mean}} = 10$ cm and $\Delta z_{\text{mean}} = 13$ cm). In the following, the mesh is refined by 2 in both directions and the consequences on the simulation results are observed. This mesh is now characterized by: $\Delta x_{\text{mean}} = 5$ cm and $\Delta z_{\text{mean}} = 6.5$ cm and keeping the same optimum Courant number entails also a time step divided by 2. The refined mesh is then 4 times bigger in memory space and 8 times longer in computing time.

4.1. Simulation results

Except the mesh, this case is entirely similar to the reference case.

To make the comparison between the reference case and the refined one, easier, the results are summarized in the Table III.

4.2. Discussion

As it was done for the reference case, the comparison with available experimental data can only be performed for the pressure drop in the bed which is quite close to the numerical value. On the other hand, the grid refinement does not affect the global behaviour of the flow, defined by parameters as mean solid volumetric fraction, pressure drop or bed height. Again, the time average of the instantaneous velocity field shows two recirculating loops. The maximal upward vertical gas and particle velocities are nearly identical to the reference case results while the downward vertical velocities along the wall are nearly two times larger. From the mesh independence of the upward vertical gas and particle velocities, we can assume that the whole recirculation flow rate is not affected by the mesh size. The downward vertical velocities are two times higher in the refined case, but the predicted downward mass flows are therefore observed over the half of the width of the reference case. So it would be very interesting to measure this downward mass flow thickness experimentally. Nevertheless, these velocities look very large considering the present experimental knowledge of the process. The effects of some additional physical mechanisms, such as inelastic particle bouncing or dynamic friction with the wall, should be then evaluated [15]. Besides, the mean solid volumetric fraction field appears less homogeneous with the refined mesh than with the reference one. Some zones of accumulation are noticeable at the bottom corners of the reactor.

Table IV. Simulation results for few values of e_c.

	Reference case		
	$e_c = 0.9$	$e_c = 0.6$	$e_c = 0.95$
Bed height (m)	8.0	8.0	8.0
Mean solid volumetric fraction	0.34	0.33	0.34
Pressure drop (3.5–6.5 m) (mbar)	85	83	85
Maximal time averaged gas velocity (upwards) (m/s)	3.9	3.8	3.9
Maximal time averaged gas velocity (downwards) (m/s)	−2.0	−2.1	−2.4
Maximal time averaged particle velocity (upwards) (m/s)	2.4	2.3	2.4
Maximal time averaged particle velocity (downwards) (m/s)	−2.6	−2.6	−3.0

From all the results and the available parameters for the experimental validation, the mesh used for the reference case seems to give precise enough results for a reasonable computing time, even if the refined case shows more detailed structures of the flow (filaments, bubbles, etc.). Further studies would be needed to quantify the influence of these small structures and if necessary to model them as subgrid effects.

5. SENSITIVITY TO THE INELASTIC RESTITUTION COEFFICIENT

The inelastic restitution coefficient e_c, given in the frame of the hard sphere collision model, describes the kinetic energy dissipation induced by the collisions between particles and is equal to 1 for elastic collisions. This parameter is not easily measured and, for modelling approaches developed in the frame of dry granular medium theory, is generally found to have a great influence on the flow. A sensitivity analysis to the e_c value has been performed for the reference. Hopefully, Table IV shows a very low sensitivity, which is explained by the fact that, in our approach, dissipation effect is induced both by the friction with the gas (the drag force) and the inter-particle collisions, these two effects tending to compensate each other.

6. SENSITIVITY TO THE SCALE-UP

One of the main goals of CFD simulations is to give information of what occurs during the scaling-up procedure: from the pilot reactor to the industrial one. So the code was used to model a pilot reactor running at the Lavéra site and being at about one-third scale of the industrial reactor.

The gas consists of hydrocarbons with a density and a kinetic viscosity of respectively about $\rho_g = 20\,\mathrm{kg/m^3}$ and $v_g = 2 * 10^{-7}\,\mathrm{m^2/s}$, at 80°C and 20 atm. The dispersed phase consists of spherical particles whose mean diameter is supposed equal to about 700 μm with a shape factor of 0.7. The equivalent diameter is then equal to 490 μm ($D_e = d_P * f$). The density of the solid is $\rho_p = 850\,\mathrm{kg/m^3}$. The superficial fluidization velocity is chosen from experimental observations to have the same fluidization regime as in the industrial reactor. The total catalytic mass is around $1800\,\mathrm{kg/m^2}$.

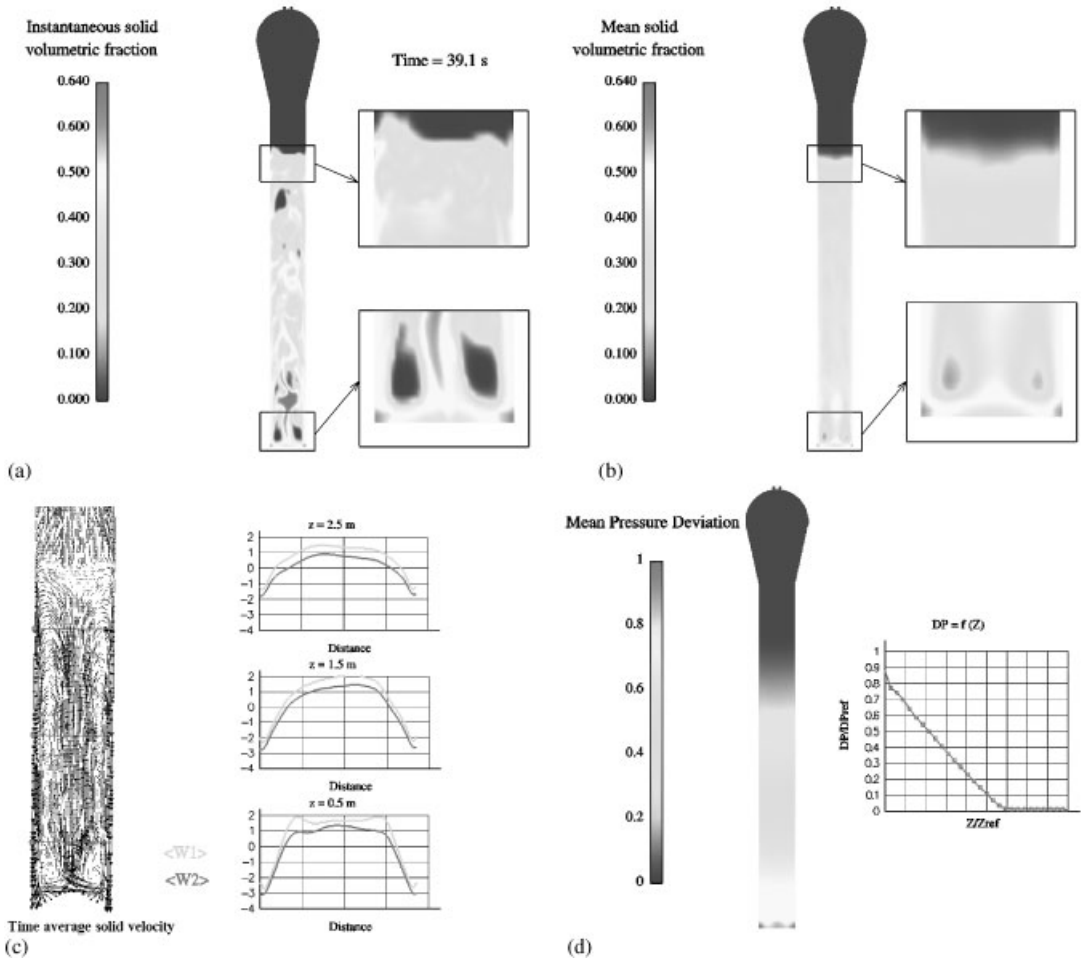

Figure 7. Simulation results of the pilot reactor.

6.1. *Simulation results*

The simulation results of the pilot reactor are shown in Figure 7.

6.2. *Discussion*

The global behaviour is very close to the one observed experimentally. The height of the bed is about 30% higher than the experimental value. At the opposite of the industrial reactor, the pilot one aims at studying the two-phase flow in the reactor. Some measurements of pressure all along the reactor were done and allow us a more precise validation, as it is shown in Figure 8. The overestimation of the height of the bed will lead to a further study to improve the characterization of the equivalent mean diameter which is found to have a major influence on the predicted bed height through the drag force modelling. For example, the shape factor is

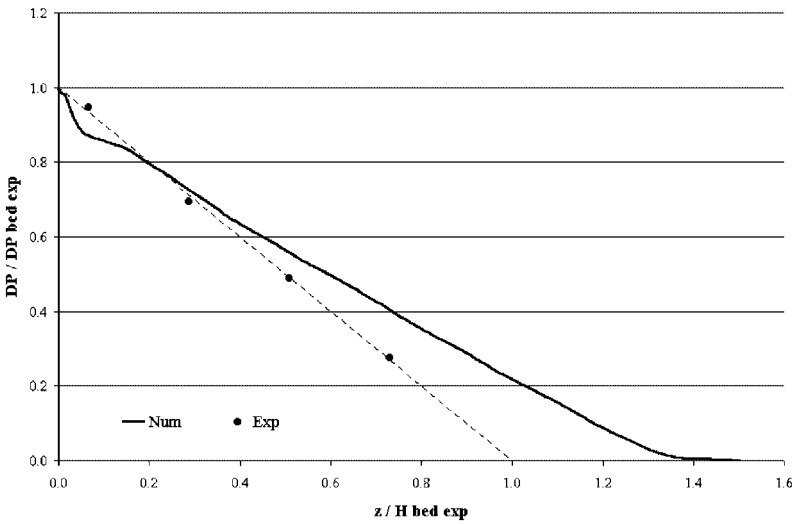

Figure 8. Dimensionless pressure profiles for the pilot reactor.

computed using the Ergun's law from experimental measurements carried out in the minimum fluidization regime, very far from the operating conditions.

Two areas of lack of particle are remarkable at the bottom of the reactor and correspond to centrifugation effects by the recirculations due to the downward flow along the wall and the gas inlet at the bottom of the reactor. Linked to this, solid accumulations are present in the corners. This aspect is a key issue because accumulation of catalyst can entail hot spots and formation of aggregates that can disturb the reactor running.

7. 3D SIMULATION

The 3D simulations were worked out quite early in this study. It was important to check that 3D effects were not predominant on the global flow behaviour and that 2D cases allowed realistic predictions for a much lower computing effort.

7.1. Presentation of the case

The conditions of this simulation are the same as the reference case ones presented in part 3. The mesh, presented by Figure 9, is structured and consists in $45*121*45$ cells (width$*$height$*$depth), i.e. $\Delta x_{\text{mean}}=11$ cm, $\Delta y_{\text{mean}}=11$ cm and $\Delta z_{\text{mean}}=20$ cm.

7.2. Simulation results

Figure 10(a) gives us a 2D-cut of the reactor which corresponds to the middle of the fluidized bed. The instantaneous solid volumetric fraction field seems to be qualitatively the same as the 2D reference case. A few parameters were compared in Table V.

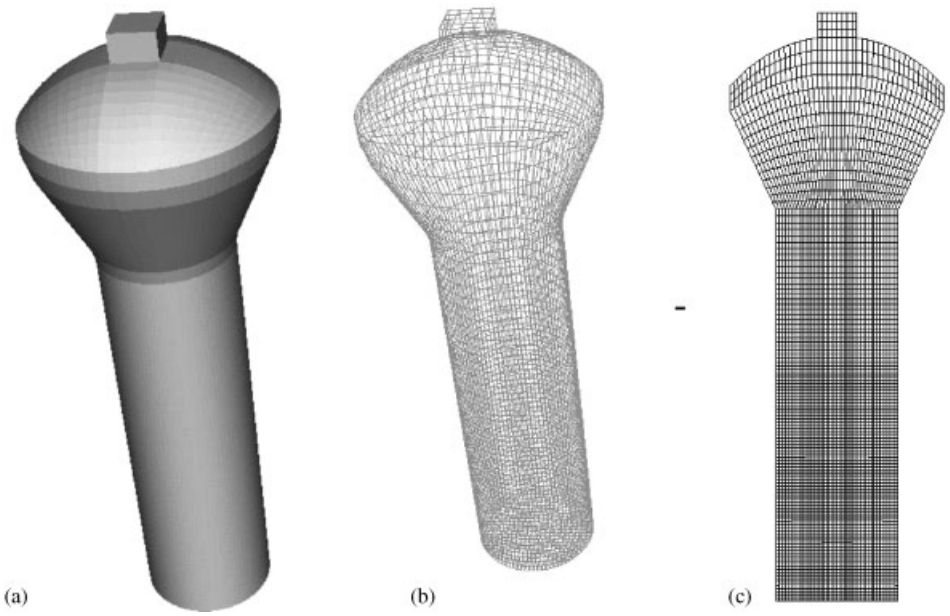

Figure 9. 3D mesh.

The 3D aspect has an influence on the bed height but the global physical behaviour of the bed remains pretty much the same. It can however be noticed that there are less bubbles than in the 2D case. That may be due to the chosen way to represent the results. Indeed, the bubbles can be present but out of the middle plane, chosen to show the simulation outcomes. Nevertheless, the 2D simulations can give good results and are a good prediction of the 3D reactor behaviour, for a much lower computing effort.

8. CONCLUSION

This study is the first step in the application of CFD for the prediction of hydrodynamic in a gas phase olefin polymerization reactor. The physical modelling and numerical code, initially developed by EDF for CFB boiler simulations, were used in their standard version. The only adjustable parameters are the mean particle diameter and the inelastic restitution coefficient. The first parameter was determined from experimental measurements and sensitivity studies have shown the very low dependence of the numerical results on the second one.

Calculations were carried out for industrial and pilot reactors, with two- and three-dimensional meshes. The results are time-dependent and their analysis was based on time averaged values over 50 s. The time averaged structure of the flow with recirculation loops and downward flow along the walls agrees with the qualitative experimental knowledge of the process. The comparison with the available pressure drop measurement shows a reasonable agreement between numerical simulation results and experimental measurements. These first results are satisfying but need further experimental validation that is ongoing on a laboratory

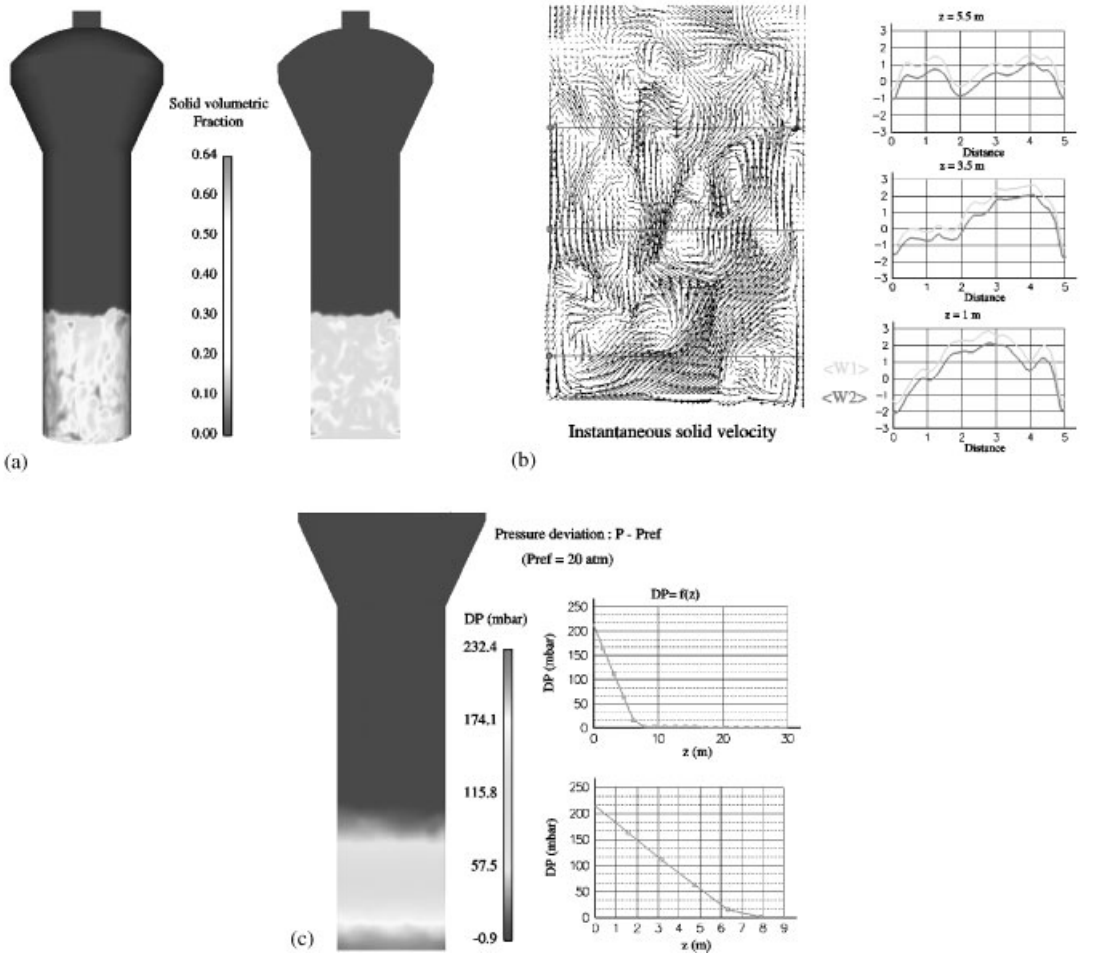

Figure 10. 3D Simulation results.

Table V. Simulation results of the 3D case.

	2D Reference case	3D case
Bed height (m)	8.0	7.0
Mean solid volumetric fraction	0.34	0.39
Pressure drop (3.5–6.5 m) (mbar)	85	95
Maximal time averaged gas velocity (upwards) (m/s)	3.9	4.4
Maximal time averaged gas velocity (downwards) (m/s)	−2.0	−1.3
Maximal time averaged particle velocity (upwards) (m/s)	2.4	3.1
Maximal time averaged particle velocity (downwards) (m/s)	−2.6	−1.8

scale reactor but in operating conditions representative of the industrial flow conditions (pressure, fluidization regime, etc.). Nevertheless, special care is needed in the characterization of the mean diameter which is found to have a great influence on the bed height and pressure drop. The closure modelling for the particle and fluid effective stresses have an effect only on the structure of the flow in the bed and so on the mixture characteristics of the bed. Simultaneously, theoretical and numerical developments will be carried out to introduce polydispersion and mass and heat interphase transfers in the modelling approach [16, 17].

NOMENCLATURE

C_β	Crossing-trajectory coefficient
$\bar{d}$	Mean diameter of the solid inclusions
D_{12}^t	Fluid-inclusion turbulent dispersion coefficient
e_c	Restitution coefficient of particle-particle collisions
F_D	Average drag coefficient
g_i	i-component of gravity
g_0	Particle pair correlation function
$I_{k,i}$	Mean interphase momentum transfer rate for phase k
K_2^{kin}	Kinetic dispersion coefficient of fluctuating particle kinetic energy
K_2^{col}	Collisional dispersion coefficient of fluctuating particle kinetic energy
P_1	Pressure of the gas phase
q_k^2	Turbulent or fluctuating kinetic energy of the phase k
q_{12}	Covariance of the fluid-particle velocity turbulent fluctuations
$u_{k,i}$	i-component of instantaneous velocity of phase k
$U_{k,i}$	i-component of mean velocity of phase k
$u''_{k,i}$	i-component of velocity fluctuation of phase k
$V_{d,i}$	Fluid-particle turbulent drift velocity
$V_{r,i}$	Mean relative velocity between the two phases

Greek letters

α_k	Fraction rate of the phase k
α_m	Maximum solid volumetric fraction equal to 0.64 for random stacking of spheres
δ_{ij}	Kronecker symbol
ε_k	Dissipation rate of turbulent kinetic energy of phase k
ε_{12}	Dissipation rate of fluid-particle covariance
ν_2^{kin}	Kinetic viscosity of the dispersed phase due to kinetic stress
ν_2^{col}	Collisional viscosity of the dispersed phase due to collisional stress
ν_1^t	Turbulent viscosity of gas phase
ν_{12}^t	Fluid-particle turbulent viscosity
ξ_c	Granular kinetic theory parameter (kinetic dispersion)
Π_{q1}	Fluid-inclusion turbulent interaction source term for the turbulent kinetic energy of the continuous phase

Π_{q2} Source term of particle interactions with fluid-turbulence
Π_{q12} Source term of fluid-particle correlations
Π_{ε} Fluid-inclusion turbulent interaction source term for the turbulent dissipation of the continuous phase
ρ_k Density of phase k
σ_c Granular kinetic theory parameter (kinetic viscosity)
$\Theta_{k,ij}$ Collisional stress tensor
τ_1^t Time macroscale of the gas turbulence or turbulent dissipation time
τ_{12}^t Time macroscale of the gas turbulence viewed by the particles or eddy-particle interaction time
τ_{12}^F Characteristic time scale of particle entrainment by the fluid motion or particle relaxation time
τ_2^c Characteristic time scale of particle-particle collisions or interparticle collision time

ACKNOWLEDGEMENTS

Some of the numerical simulations were performed at the computing centre of Calmip (Calcul en Midi-Pyrénées) in the frame of project P0111.

REFERENCES

1. Thai Van D, Minier JP, Simonin O, Freydier P, Olive J. Multidimensional two-fluid model computation of turbulent dispersed two-phase flows. *Proceedings of the International Symposium on Numerical Methods for Multiphase Flows*, vol. 185. ASME FED 1994; 277–291.
2. Lun C, Savage SB, Jeffrey DJ, Cherpurniy N. Kinetic theories of granular flow: simple shear of inelastic particles and general deformations of nearly elastic particles. *Journal of Fluid Mechanics* 1984; **140**:223–256.
3. Jenkins JT, Richmann MW. Grad's 13-moment system for a dense gas of inelastic spheres. *Archive for Rational Mechanics and Analysis* 1985; **87**:355–377.
4. Ding J, Gidaspow D. A bubbling fluidization model using kinetic theory of granular flow. *A.I.Ch.E. Journal* 1990; **36**(4):523–538.
5. Simonin O. Prediction of the dispersed phase turbulence in particle-laden jets. *Proceedings of the 4th International Symposium on Gas-Solid Flows*, vol. 121. ASME FED 1991; 197–206.
6. He J, Simonin O. Non-equilibrium prediction of the particle-phase stress tensor in vertical pneumatic conveying. *Proceedings of the 5th International Symposium on Gas-Solid Flows*, vol. 166. ASME FED 1993; 253–263.
7. Balzer G, Simonin O, Boëlle A, Laviéville J. A Unifying modelling approach for the numerical prediction of dilute and dense gas–solid two-phase flows. In *Circulating Fluidized Bed Technology V*, *Proceedings of the 5th International Conference on Circulating Fluidized Beds*, Kwauk M, Li J (eds). Science Press: Beijing, 1996; 432–439.
8. Balzer G, Boëlle A, Simonin O. Eulerian gas–solid flow modelling of dense fluidized bed. *FLUIDIZATION VIII*, *Proceedings of the International Symposium of the Engineering Foundation*, Large JF, Laguérie C (eds). 1995; 409–418.
9. Delloume V, Peirano E, Johnsson F, Leckner B, Simonin O. Numerical simulation of the fluid dynamics of a freely bubbling fluidized bed: influence of the air supply system. *Powder Technology* 2002; **122**:69–82.
10. Peirano E, Delloume V, Leckner B. Two- or three-dimensional simulations of turbulent gas–solid flows applied to fluidization. *Chemical Engineering Science* 2001; **56**:4787–4799.
11. Wen CY, Yu YH. Mechanics of fluidization. *Chemical Engineering Symposium Series* 1965; **62**:100–111.
12. Simonin O. Statistical and continuum modelling of turbulent reactive particulate flows. Part 1: theoretical derivation of dispersed Eulerian modelling from probability density function kinetic equation. *Theoretical and Experimental Modelling of Particulate Flows*, Lecture Series 2000-06, von Karman Institute for Fluid Dynamics, Rhode Saint Genése, Belgium, 2000.
13. Campbell CS. Rapid granular flows. *Annual Reviews in Fluid Mechanics* 1990; **22**:57–92.
14. Boëlle A, Balzer G, Simonin O. Second-order prediction of the particle-phase stress tensor of inelastic spheres in simple shear dense suspensions. *Proceedings of the 6th International Symposium on Gas-Solid Flows*, vol. 228. ASME FED 1995; 9–18.

15. Sakiz M, Simonin O. Development and validation of continuum particle wall boundary conditions using Lagrangian simulation of a vertical gas–solid channel flow. *Proceedings of the 8th International Symposium on Gas-Particle Flows*, ASME Fluids Engineering Division Summer Meeting, FEDSM99-7898, 1999.
16. Gourdel C, Simonin O, Brunier E. Two-Maxwellian equilibrium distribution function for the modelling of a binary mixture of particles. *Circulating Fluidized Bed Technology VI*, *Proceedings of the 6th International Conference on Circulating Fluidized Beds*, Werther J (ed.). DECHEMA, Frankfurt am Main: Germany, 1999; 205–210.
17. Albrecht A, Simonin O, Barthod D, Vedrine D. Multidimensional numerical simulation of the liquid feed injection in an industrial FCC riser. *FLUIDIZATION X*, *Proceedings of the International Symposium of the Engineering Foundation*, Beijing, China, 2001.

